

Manipulating Current-Induced Magnetization Switching

S. Urazhdin

Department of Physics and Astronomy, Johns Hopkins University, Baltimore, MD, 21218

H. Kurt, M. AlHajDarwish, Norman O. Birge, W. P. Pratt Jr., and J. Bass

Department of Physics and Astronomy, Center for Fundamental Materials Research and Center for Sensor Materials, Michigan State University, East Lansing, MI 48824

We summarize our recent findings on how current-driven magnetization switching and magnetoresistance in nanofabricated magnetic multilayers are affected by varying the spin-scattering properties of the non-magnetic spacers, the relative orientations of the magnetic layers, and spin-dependent scattering properties of the interfaces and the bulk of the magnetic layers. We show how our data are explained in terms of current-dependent effective magnetic temperature.

PACS numbers: 73.40.-c, 75.60.Jk, 75.70.Cn

I. INTRODUCTION

Since the discovery of current-induced magnetization switching (CIMS) in magnetic nanopillars [1, 2], researchers have investigated the effects of temperature [3, 4], external magnetic field H [4, 5, 6], layers' thicknesses [6], interlayer interactions [7, 8], and magnetic moment density [9]. The interest for such studies is twofold. For technological applications, it is necessary to minimize the switching currents for CIMS use in memory devices, or, on the contrary, minimize the current-induced noise in field sensors. From the fundamental point of view, CIMS allows one to access the strongly out of equilibrium magnetic dynamics, and study the interaction of magnetization with conduction electrons and phonons. In Section II, we summarize our recent studies of how various modifications of the basic ferromagnetic-nonmagnetic-ferromagnetic ($F_1/N/F_2$) trilayer structure used for CIMS affect the switching currents I_s and the magnetoresistance $\Delta R = R_{AP} - R_P$ [10, 11, 12]. Here, $R_{(AP)P}$ is the resistance of the state with (anti)parallel magnetizations of F_1 and F_2 . First, we enhance ΔR in Py/Cu/Py (Py=Permalloy= $\text{Ni}_{84}\text{Fe}_{16}$) trilayer nanopillars by inserting 1 nm of a strong spin-scatterer, $\text{Fe}_{50}\text{Mn}_{50}$ [13] between the trilayer and the top electrode. Second, we insert a t_{CuPt} thick $\text{Cu}_{94}\text{Pt}_6$ layer between the Py layers. The short spin-diffusion length in $\text{Cu}_{94}\text{Pt}_6$ decreases ΔR [13]. Third, we study the variation of ΔR and I_s with the angle between the magnetizations of the two ferromagnetic layers in Py/Cu/Py nanopillars. Fourth, we dope Ni or Fe with Cr for F_1 and/or F_2 to induce predominantly majority electron scattering in the bulk of ferromagnets, or use Cr spacer with Fe to give predominantly majority electron scattering at F/N interface [14]. Finally, in Section III we demonstrate that all our results are consistent with the effective magnetic temperature model (EMT) of Ref. [15].

II. EXPERIMENT

Our samples were made with a multistep process described elsewhere [7]. Below, all thicknesses are in nanometers. The basic samples had structure $\text{Cu}/F_1/N/F_2/\text{Au}$. In addition to the modifications specified for each sample below, in some samples a thin Cu spacer was inserted between F_2 and the top Au. The Cu/F_1 layers were thick extended bottom leads. N and F_2 were patterned into an elongated shape with typical dimensions $\approx 130 \times 70$ nm (nanopillar). Au was a thick top lead. Leaving F_1 extended minimized the effect of dipolar coupling on the current-driven switching [7], and N was sufficiently thick to minimize exchange coupling between F_1 and F_2 . We measured dV/dI at room temperature (295 K) with four-probes and lock-in detection, adding an ac current of amplitude 20–40 μA at 8 kHz to the dc current I . Positive current flows from the extended to the patterned Py layer. The field H is in the film plane and (except for the angular dependence studies) along the nanopillar easy axis.

A. Enhancing CIMS

Fig. 1(a) shows typical CIMS results for a sandwich $F_1=\text{Py}(30)/N=\text{Cu}(15)/F_2=\text{Py}(6)/\text{Cu}(2)$ (sample of type 1). In samples of type 2, the top $\text{Cu}(2)$ layer was replaced with a $\text{Cu}(2)/\text{Fe}_{50}\text{Mn}_{50}(1)/\text{Cu}(2)$ sandwich (Fig. 1(b)). The typical switching fields, H_s (insets Fig. 1) were similar for both sample types. For 14 samples of type 1, $\Delta R \equiv R_{AP} - R_P = 0.060 \pm 0.002\Omega$. $I_s^{AP \rightarrow P} = -2.45 \pm 0.2$ mA, and $I_s^{P \rightarrow AP} = 3.8 \pm 0.2$ mA are the switching currents from AP to P, and from P to AP state, respectively. For 12 samples of type 2, $\Delta R = 0.085 \pm 0.012\Omega$, $I_s^{AP \rightarrow P} = -1.5 \pm 0.2$ mA, and $I_s^{P \rightarrow AP} = 1.85 \pm 0.2$ mA. For uncertainties, we give twice the standard deviations of the mean. Thus, insertion of FeMn outside the Py/Cu/Py trilayer reduces the average $I_s^{AP \rightarrow P}$ by a factor of ≈ 1.6 , and $I_s^{P \rightarrow AP}$ by 2.1. The increase of ΔR results from the enhancement of spin-

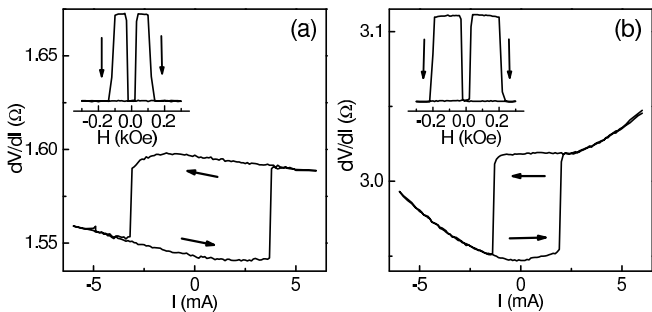


FIG. 1: (a) dV/dI vs. I for a sample of type 1 (as defined in the text) at $H = 0$. Inset: dV/dI vs. H at $I = 0$. (b) Same as (a), for a sample of type 2. (From Urazhdin *et al.* [10])

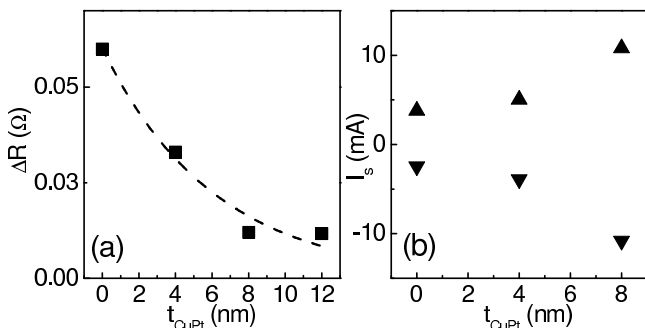


FIG. 2: (a) Variation of ΔR with t_{CuPt} . Dashed line is a fit with $\Delta R = \Delta R_0 \exp[-t_{CuPt}/l_{sf}^{CuPt}]$, $\Delta R_0 = 0.060 \pm 0.004 \Omega$, $l_{sf}^{CuPt} = 6.1 \pm 0.8$ nm. (b) $I_s^{P \rightarrow AP}$ (upward triangles) and $I_s^{AP \rightarrow P}$ (downward triangles) vs. t_{CuPt} . (From Urazhdin *et al.* [10])

accumulation in the trilayer, due to the spin-memory loss in FeMn(1) [13]. The associated decrease of I_s indicates the importance of spin-accumulation for CIMS.

B. Suppressing CIMS

Sample types 3-5 had the structure of sample type 1, except $N=Cu(15)$ was replaced with $Cu(13.5-d)/Cu_{94}Pt_6(d)/Cu(1.5)$, with $d=4, 8,$ and 12 , respectively. Fig. 2 shows data for sample types 1, 3, 4, 5. Fig. 2(a) ($\Delta R(t_{CuPt})$) gives a spin-diffusion length of 6.1 ± 0.8 nm in $Cu_{94}Pt_6$ at 295 K, shorter than ≈ 10 nm at 4.2 K [13]. Fig. 2(b) shows that both $I_s^{P \rightarrow AP}$ and $|I_s^{AP \rightarrow P}|$ increase with increasing t_{CuPt} . Interestingly, the ratio $Q = I_s^{P \rightarrow AP}/|I_s^{AP \rightarrow P}|$ decreases from ≈ 1.5 at $t_{CuPt} = 0$ to ≈ 1.0 for $t_{CuPt} = 8$. This decrease with increased spin-flipping within the N-layer is opposite to that reported in [6] for a similar measurement with varied thickness of $N=Cu$, and is inconsistent with the explanation proposed there.

The inset of Fig. 3(a) illustrates that all 8 samples of type 5 showed hysteretic field-driven switching, simi-

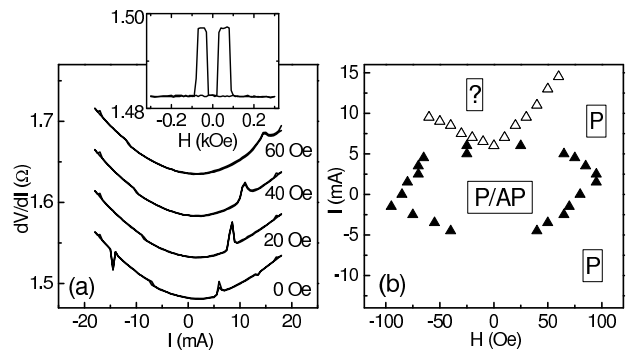


FIG. 3: Data for a sample of type 5: (a) dV/dI vs. I . Inset: dV/dI vs. H . (b) Stability diagram, obtained from H-scans at various fixed I (solid symbols), and I-scans at fixed H (open symbols). P is the region where only the P state is stable, P/AP is a bistable region, and the region labeled [?] is the inhomogeneous magnetization state. (From Urazhdin *et al.* [12])

lar to the other sample types. However, none exhibited reproducible hysteretic current-switching. As Fig. 3(a) shows for $H = 0$ to 60 Oe, the current dependencies exhibit reversible switching peaks at small H , rapidly moving to higher I at larger H . The resistance change associated with such peaks indicates switching between the P state and an inhomogeneous magnetization state, likely affected by the current-induced Oersted field. In Fig. 3(a), P to inhomogeneous state switching without a peak also occurs at $H = 0$, $I = -7$ mA, with a partial reverse transition at $I = -14.5$ mA (downward peak). In some of the other samples of type 5, a switching peak appears only at $I < 0$, or in both directions of I . Averaging among 8 samples, at $H = 0$ the peaks appeared at $|I| \approx 10$ mA. Fig. 3(b) shows why CIMS is absent in these samples: When I is reduced from a large positive value at small H , the magnetization M_2 of F_2 switches reversibly from the inhomogeneous to the P state (as I crosses the line marked by open symbols), then goes through the P/AP and P regions without changing. The AP state is achieved only by flipping the magnetization M_1 of F_1 with H . The results of Fig. 3 are important in the context of attempts to understand the current-driven behavior of a single magnetic layer [16, 17, 18]. By placing a thick CuPt layer in the spacer between two Py layers, we approached a single-layer regime, while retaining a small ΔR necessary to determine the orientation of M_2 . An approximate symmetry of the effects of positive and negative currents (Fig. 3) shows that, indeed, the switching of M_2 is not significantly affected by M_1 .

C. Noncollinear Switching

Fig. 4 shows the results for varied non-collinear orientations of magnetic layers in sample type 1. These data confirm results reported in [19], but with a larger mag-

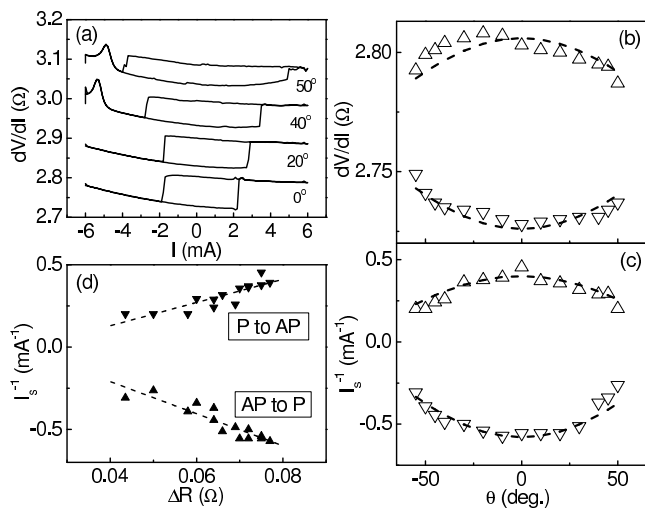


FIG. 4: (a) CIMS for various non-collinear orientations of M_1 and M_2 , as labeled. Curves are offset for clarity. (b) Quasi-parallel (P) and quasi-antiparallel (AP) state resistances R_P (upward triangles) and R_{AP} (downward triangles) vs. θ . Dashed curves: fits as explained in the text. (c) $1/I_s^{P \rightarrow AP}$ (upward triangles) and $1/I_s^{AP \rightarrow P}$ (downward triangles) vs. θ . Dashed curves: fits as explained in the text. (d) $1/I_s$ vs. ΔR for noncollinear switching, dashed lines are best linear fits.

netoresistance $\Delta R/R$. Before each measurement, a pulse of $H = 60$ Oe at the desired in-plane angle θ was applied to rotate M_1 parallel to H , then the current-switching was measured at $H = 10$ Oe, needed to fix M_1 . Fig. 4(a) shows that for $\theta < 60^\circ$ the switching occurred though a well defined sharp step, at increasing I_s and decreasing ΔR with increasing θ . At larger θ , the switching points became poorly defined. They are not included in Fig. 4. Fig. 4(b) shows that the resistance of the quasi-parallel state increased, and the quasi-antiparallel state decreased when $|\theta|$ increased. Dashed curves are fits assuming $R_{P,AP} = R_0 \mp A \cos \theta$, $R_0 = 2.77 \Omega$, $A = 0.04 \Omega$, as justified in Section III. $\Delta R \approx 2A = 0.08 \Omega$ for the collinear magnetoresistance of this sample. Dashed curves in Fig. 4(c) for the inverse switching currents are fits with $1/I_s^{P \rightarrow AP, AP \rightarrow P} = K_{P,AP} \cos \theta$, $K_P = 0.40 \text{ mA}^{-1}$, $K_{AP} = -0.58 \text{ mA}^{-1}$. Here $K_P \approx 1/I_s^{P \rightarrow AP}$ and $K_{AP} \approx 1/I_s^{AP \rightarrow P}$ for the CIMS with collinear magnetizations. Dashed lines in Fig. 4(d) for the $1/I_s$ vs. ΔR are best linear fits. Their intercepts with $1/I_s = 0$ axis are at finite ΔR .

In Fig. 5, we plot average $1/I_s$ vs. average ΔR using the data of Figs. 1-4. The uncertainties are close to the symbol sizes in Fig. 5. The overall agreement for three different types of measurements suggests a general inverse relationship between I_s and ΔR , independent of the particular way in which ΔR was varied. The switching is determined by the current density, so both $1/I_s$ and ΔR are inversely proportional to the nanopillar areas; their variation only leads to scaling along the approximately linear dependence in Fig. 5(a). The solid lines show best

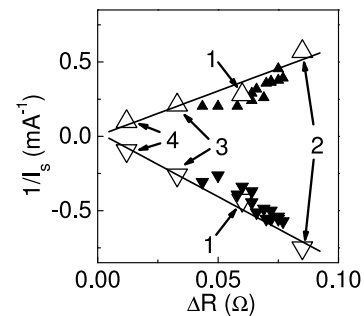


FIG. 5: Dependence of $1/I_s^{P \rightarrow AP}$ (upward triangles) and $1/I_s^{AP \rightarrow P}$ (downward triangles) on ΔR . Open symbols: sample types 1 through 4, as labeled. Solid symbols: variations with angle between the magnetizations in a sample of type 1. Solid lines: best linear fits of data, excluding the angular dependence. (From Urazhdin *et al.* [10])

linear fits, excluding the angular dependence data. The ordinate intercepts of both fits are zero within the uncertainty of the fits.

D. Inverting Magnetoresistance and/or CIMS

In sample types 1-5, the minority electrons (i.e. with moments antiparallel to the layers' magnetizations) were always scattered more strongly both in the bulk of F_1 and F_2 and at their interfaces. Fig. 6 demonstrates the effects on ΔR and CIMS of inverting the scattering anisotropies [11].

Fig. 6(a) is for $F_1 = \text{Ni}_{97}\text{Cr}_3(20)/\text{N} = \text{Cu}(20)/F_2 = \text{Py}(10)$ (sample type 6). By doping Ni with Cr, we inverted the anisotropy of F_1 , so that majority electrons are scattered in F_1 more strongly than the minority ones. Inset of Fig. 6(a) shows that ΔR is inverted (as compared to normal ΔR in samples of type 1), i.e. $R_P > R_{AP}$. CIMS in Fig. 6(a) looks qualitatively similar to Fig. 1, but inverted ΔR means that CIMS is actually also inverted, i.e. $I > 0$ gives switching to the high resistance P state, and $I < 0$ gives switching to the low resistance AP state.

Fig. 6(b) is for $F_1 = \text{Fe}_{95}\text{Cr}_5(20)/\text{N} = \text{Cr}(6)/F_2 = \text{Fe}_{95}\text{Cr}_5$ (sample type 7). The bulk and interfaces of ferromagnets with Cr all scatter the majority electrons more strongly. Inset of Fig. 6(b) shows that the sign of ΔR is the same as for samples of type 1, as is always the case for symmetric trilayers. CIMS in Fig. 6(b) is inverted.

Fig. 6(c) is for $F_1 = \text{Py}(20)/\text{N} = \text{Cu}(7)\text{Cr}(3)/F_2 = \text{Fe}_{95}\text{Cr}_5$ (sample type 8). In this case, F_1 and F_1/N have positive anisotropy, but F_2 and F_2/N have negative anisotropy. Inset in Fig. 6(c) shows that ΔR is inverted. CIMS also looks inverted compared to samples of type 1, but since ΔR is inverted, CIMS is actually the same, i.e. $I > 0$ gives the low-resistance AP state, and $I < 0$ gives the high-resistance P state.

In summary, samples 1,6-8 demonstrate all 4 possible combinations of signs of ΔR and CIMS: labeling these

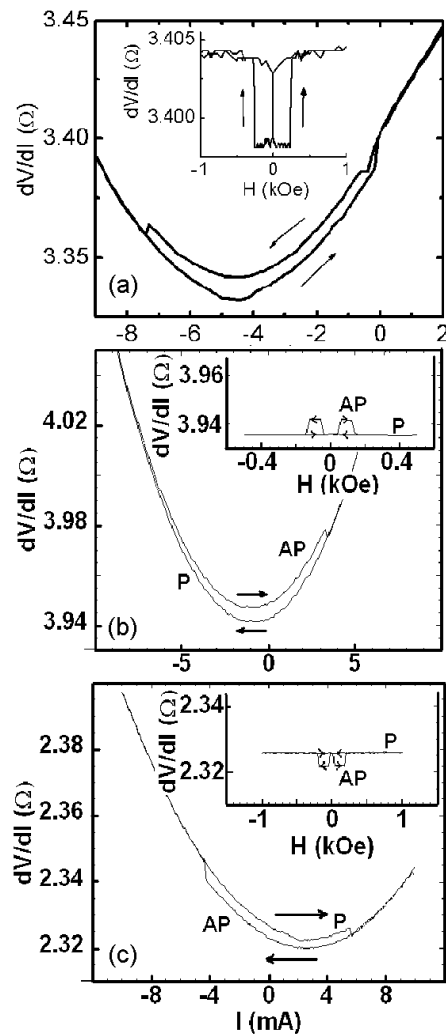


FIG. 6: (a-c) dV/dI vs. I for samples of types 6-8, correspondingly. Insets: dV/dI vs. H . (b), (c) are from AlHaj-Darwish *et al.* [11].

signs normal in sample type 1, samples of type 6 show inverted ΔR and inverted CIMS, samples of type 7 show normal ΔR and inverted CIMS, and samples of type 8 show inverted ΔR and normal CIMS.

III. MODEL AND ANALYSIS

The generally accepted spin-transfer torque model (STT) for CIMS is usually combined with the macrospin current-driven magnetization dynamics [20, 21]. Finite-temperature analysis showed that the effect of STT on the macrospin dynamics is equivalent to renormalization of temperature T , giving [22, 23]

$$T'(I) = \frac{T}{1 + pI'\hbar/(2em\alpha H_{eff})}, \quad (1)$$

where α is the Gilbert damping parameter, $H_{eff} \approx H + 2\pi M_2$, and m is the magnetic moment of F_2 . We

show elsewhere [15, 24] that I' should be generally understood as the current through the nanopillar if electron scattering on F_2 were absent, and p is that current's polarization. T' was treated in Refs. [22, 23] as a formal parameter for the current-dependence of the switching rate $\Omega(I) = \Omega_0 \exp[-U/kT'(I)]$, where $\Omega_0 \approx 10^{-9}$ sec is the switching attempt rate, and U is the switching barrier determined by the anisotropy field of the nanopillar. Furthermore, it can be shown that T' is the actual magnetic temperature of the macrospin, defined by the probability distribution of its orientation [23, 24].

STT has been recently extended to inhomogeneous dynamical states [16] and incorporated in micromagnetic models [25, 26, 27]. Micromagnetic simulations invariably show that CIMS occurs through inhomogeneous intermediate magnetic states, not adequately described by the macrospin approximation even in nanostructures. We introduced effective magnetic temperature (EMT) to collectively describe such inhomogeneous dynamical states [4, 15]. Surprisingly, an apparently different approximation used by EMT gives an expression similar to Eq. 1. We show elsewhere [24] that contrary to the claim of Ref. [15], this similarity is not accidental: incoherent excitation of finite wavelength modes simply gives larger H_{eff} in Eq. 1, reflecting higher average damping rates of finite-wavelength excitations. We shall see below that macrospin calculations underestimate the switching currents by an order of magnitude, or equivalently require unrealistically large Gilbert damping α , to compensate for the higher H_{eff} associated with nonuniform magnetic dynamics.

Here, we use a simplified quasi-ballistic approach for electron scattering in the nanopillar, and Eq. 1 to explain our data. Following Ref. [15], we approximate the nanopillar by a high-resistance constriction separating low-resistance reservoirs. Only F_2 is contained in the constriction, F_1 and various nonmagnetic inserts such as $\text{Cu}_{94}\text{Pt}_6$ or $\text{Fe}_{50}\text{Mn}_{50}$, if present, are part of the reservoirs. To model the polarizing effect of F_1 , we introduce different spin-up and spin-down potentials in the left reservoir containing F_1 , V^\uparrow , V^\downarrow , which are determined by the magnetic orientation F_1 and the properties of spacer, e.g. spin-memory loss in $\text{Cu}_{94}\text{Pt}_6$. This approximation is equivalent to introducing different numbers of channels for spin-up and spin-down electrons in Landauer-Buttiker formalism, physically justified by the spin-dependent band structure of F_1 . We neglect spin-accumulation in the right reservoir, i.e. take $V = 0$ there. I^\uparrow , I^\downarrow are spin-up and spin-down currents through the constriction. Positive currents are from F_1 to F_2 . Spin states are defined with respect to the magnetization M_2 of F_2 . We define ΔV , p by $\Delta V = V^\uparrow - V^\downarrow = 2pV$. Here $V \approx (V^\uparrow + V^\downarrow)/2$ is somewhat smaller than the voltage across the multilayer because of the current bunching in the leads. If F_2 is removed, p becomes the current polarization in the constriction, positive for the P state, and negative for the AP state for Py-based nanopillars. For simplicity, we approximately describe the contribu-

tion of F_1 and its interfaces and other various contact and bulk contributions to the nanopillar resistance by a resistance R_0 . Spin-dependent scattering at each of the interfaces of F_2 is described by conductances G^\uparrow, G^\downarrow , so that $V^{\uparrow(\downarrow)} = I^{\uparrow(\downarrow)}(2R_0 + 2/G^{\uparrow(\downarrow)})$. We neglect multiple scattering, so the interface resistances add. For now we also assume no spin-flip scattering in F_2 . In this approximation,

$$V = \frac{I}{\left(\frac{1+p}{2R_0 + \frac{2}{G^\downarrow}} + \frac{1-p}{2R_0 + \frac{2}{G^\uparrow}}\right)} \quad (2)$$

and

$$\Delta R = \frac{4p(R_0 + 1/G^\uparrow)(R_0 + 1/G^\downarrow)(1/G^\downarrow - 1/G^\uparrow)}{[2R_0 + 1/G^\downarrow + 1/G^\uparrow]^2 - p^2[1/G^\downarrow - 1/G^\uparrow]^2}, \quad (3)$$

approximately proportional to p .

Similarly to STT [20], we assume that all the electrons scattered by F_2 contribute equally to spin-transfer, regardless whether they are reflected or transmitted by F_2 . Only the transmitted electrons contribute to the charge current, so we need to find the relation between the current and the number of electrons scattered (i.e. either reflected or transmitted) by F_2 . In Eq. 1 for spin-transfer, pI' is the polarized current through the constriction if F_2 were absent, giving pI'/e - the difference between the numbers of electrons with spin-up and spin-down, scattered (i.e. either reflected or transmitted) by F_2 per unit time. Plugging the voltage from Eq. 2 into $pI' = pV/R_0$,

$$pI' = \frac{2pI(R_0 + 1/G^\downarrow)(R_0 + 1/G^\uparrow)}{R_0[2R_0 + 1/G^\uparrow + 1/G^\downarrow + p(1/G^\downarrow - 1/G^\uparrow)]} \quad (4)$$

We shall see below that the spin-dependent scattering by F_2 explains the asymmetry of the switching currents.

In EMT, CIMS occurs through thermal activation over an effective magnetic barrier determined by the shape anisotropy of the nanopillar [15]. For the average switching time $\tau = 1$ sec, the switching temperature is $T_0(I) \approx U/(k_B \ln \Omega_0)$, where $\Omega_0 \approx 10^9 \text{ sec}^{-1}$ is the effective attempt rate [22], and $U \approx 0.9 \text{ eV}$ is the estimated activation barrier for 6 nm thick Py nanopillars at 295 K. Approximating $U(T) \approx \sqrt{1 - T/T_c}$, where $T_c = 800 \text{ K}$ for Py, we obtain $T_0 \approx 430 \text{ K}$. We calculate the switching currents from Eq. 1 with pI' from Eq. 4

$$\frac{1}{I_s} = \frac{\hbar}{e\alpha H_{eff}(1 - T/T_0)} \times \frac{p(R_0 + 1/G^\downarrow)(R_0 + 1/G^\uparrow)}{R_0[2R_0 + 1/G^\uparrow + 1/G^\downarrow + p(1/G^\downarrow - 1/G^\uparrow)]} \quad (5)$$

Eq. 5 shows that I_s is approximately inversely proportional to the current polarization created by F_1 . The asymmetry of $I_s^{P \rightarrow AP}, I_s^{AP \rightarrow P}$ is determined by the values of R_0, G , and p , and is a consequence of the spin-dependent scattering by the nanopillar. The fundamental quantity giving CIMS is not the current, but rather the spin-dependent voltage across the nanopillar.

We perform numerical analysis with the derived equations using the statistically significant data for sample types 1-5, and give only qualitative explanations for sample types 6-8. We start with the ratio $Q = I_s^{P \rightarrow AP}/|I_s^{AP \rightarrow P}|$, which lets us find the ballast resistance R_0 . For our Py nanopillars with area $\approx 10^{-14} \text{ m}^2$, $G^\uparrow = 33 \pm 3 \text{ s}$, $G^\downarrow = 6 \pm 0.6 \text{ s}$ [28, 29]. For Py/Cu/Py samples, we estimate $p_0 = 0.6$. For $R_0 = 0$, Eq. 5 gives $Q = 2.4$. For large R_0 , $Q = 1$. $R_0 = 0.1 \text{ } \Omega$ gives $Q = 1.5$ in agreement with experiment. This value is comparable to the Sharvin resistance of the nanopillar. For samples with $\text{Cu}_{94}\text{Pt}_6$ inserts, $p \approx p_0 \exp[-t_{\text{CuPt}}/l_{sf}^{\text{CuPt}}]$ with $l_{sf}^{\text{CuPt}} = 6.1 \pm 0.8 \text{ nm}$ (Fig. 2). Eq. 5 then gives a decrease of Q from 1.5 for samples of type 1 to 1.1 in samples of type 4, in reasonable agreement with the data of Fig. 2.

Plugging realistic sample parameters into Eq. 3 gives $\Delta R = 0.07 \Omega$ for samples of type 1, in good agreement with the data. The deviations from the linear dependence on p in Eq. 3 are negligible, thus also reproducing the dependence of ΔR on t_{CuPt} for sample types 3-5.

The calculation of I_s using Eq. 5 requires estimates for the Gilbert damping parameter α , which in thin films may significantly deviate from the bulk value, and for the parameter H_{eff} , which depends on the typical energies of the magnetic modes excited by the current. For CIMS in nanopillars at small in-plane H , H_{eff} for uniform precession becomes $H_{eff} \approx 2\pi M + H$, where $M \approx 800 \text{ Oe}$ is the magnetization of Py. For $H \ll 2\pi M$, $H_{eff} \approx 5 \text{ kOe}$. The I_s data of Sec. II are reproduced with unrealistic $\alpha \approx 0.12$. Thin-film FMR measurements indicate that for our 6 nm thick Py the damping should not significantly exceed the bulk value $\alpha \approx 0.01$ [30]. Eq. 5 then gives $H_{eff} \approx 5 \text{ T}$, corresponding to typical energies $E_i \approx 0.7 \text{ meV}$ for magnons participating in the magnetization switching. Incidentally, this estimate is consistent with the conduction electron energies due to the voltage across the nanopillar. This is expected from energy conservation in the electron-magnon scattering, not considered in the STT-based models.

The corrections to the linear dependencies on p in Eqs. 3, 5 are negligible. Thus, we reproduce the inverse relationship $1/I_s \propto \Delta R \propto p$ for sample types 1,3,4, where p was varied by inserting $\text{Cu}_{94}\text{Pt}_6$. By respective rotations of the layers' magnetizations in sample type 1 (Fig. 4), we varied $p \approx p_0 \cos \theta$, where p_0 is the polarization for the collinear magnetic orientation. Eqs. 3, 5 then validate the functional forms we used for fitting those data.

We interpret the behaviors of Fig. 3 with two alternative explanations: i) the dominant effect of the unpolarized current through the nanopillar is due to its Oersted field and/or Joule heating. We speculate that these effects reduce the value of H_s , independently of the current direction; ii) unpolarized current spontaneously generates magnetic excitations, at a rate that is independent of both the current direction and the orientation of the nanopillar [15]. More detailed experiments and modeling are necessary to determine the relative importance of the

alternatives i) and ii).

Finally, the behaviors of sample types 6-8 with inverted anisotropies are explained by Eqs. 3, 5, keeping in mind that p is the polarization of current that would flow through the nanopillar if F_2 were absent. From Eq. 3, $\Delta R \propto p(1/G^\downarrow - 1/G^\uparrow)$, positive when anisotropies of F_1 and F_2 are the same (sample types 1 and 7), and negative when they are opposite (sample types 6,8), From Eq. 5, the switching current sign only depends on the anisotropy of F_1 , i.e. the sign of p : positive in sample types 1 and 8, giving normal CIMS, and negative for sample types 6 and 7, giving inverted CIMS. Our model does not include the spin-accumulation effects caused by the anisotropy of F_2 [11]. These effects are most pronounced in samples of type 6 with a highly anisotropic F_2 =Py and weakly anisotropic F_1 =Ni₉₇Cr₃, giving asymmetry of the currents for the opposite switching directions.

IV. SUMMARY

In this paper, we summarized the following important experimental observations for the variation of the magne-

tization switching current I_s with multilayer parameters: i) I_s is reduced by inserting a strongly spin-scattering layer between the magnetic trilayer and one of the leads, ii) I_s is increased by inserting a spin-scattering layer between the magnetic layers, iii) I_s is smallest when the magnetizations of the layers are collinear, iv) for a fixed switching layer, there is an approximately linear relation between the magnetoresistance and $1/I_s$, regardless of the method by which these parameters are varied, v) all four possible combinations of magnetoresistance and switching current signs are produced by manipulating with the scattering anisotropies of the magnetic layers and their interfaces. In our samples, the sign of the switching current is determined by the overall anisotropy of the fixed magnetic layer, and independent of the anisotropy of the switching layer. Finally, we show that our data are consistent with the predictions of the effective magnetic temperature model.

This work was supported by the MSU CFMR, CSM, the MSU Keck Microfabrication facility, the NSF through Grants DMR 02-02476, 98-09688, and NSF-EU 00-98803, and Seagate Technology.

-
- [1] M. Tsoi, A.G.M. Jansen, J. Bass, W.C. Chiang, M. Seck, V. Tsoi, and P. Wyder, *Phys. Rev. Lett.* **80**, 4281 (1998); **81**, 493(E) (1998).
 - [2] E.B. Myers, D.C. Ralph, J.A. Katine, R.N. Louie, R.A. Buhrman, *Science* **285**, 867 (1999).
 - [3] E. B. Myers, F.J. Albert, J.C. Sankey, E. Bonet, R.A. Buhrman, and D.C. Ralph, *Phys. Rev. Lett.* **89**, 196801 (2002).
 - [4] S. Urazhdin, N.O. Birge, W.P. Pratt Jr., and J. Bass, *Phys. Rev. Lett.* **91**, 146803 (2003).
 - [5] J. Grollier, V. Cros, A. Hamzic, J.M. George, H. Jaffres, A. Fert, G. Faini, J.B. Youssef, and H. Legall, *Phys. Rev. B* **67**, 174402 (2003).
 - [6] F. J. Albert, N.C. Emley, E.B. Myers, D.C. Ralph, and R.A. Buhrman, *Phys. Rev. Lett.* **89**, 226802 (2002).
 - [7] S. Urazhdin, H. Kurt, W.P. Pratt Jr., and J. Bass, *Appl. Phys. Lett.* **83**, 114 (2003).
 - [8] S. Urazhdin, W.P. Pratt Jr., and J. Bass, *J. Magn. Magn. Mater.* **272**, 1586 (2004).
 - [9] M.R. Pufall, W.H. Rippard, T.J. Silva, *Appl. Phys. Lett.* **83**, 323 (2003).
 - [10] S. Urazhdin, N.O. Birge, W.P. Pratt Jr., J. Bass, *Appl. Phys. Lett.* **84**, 1516 (2004).
 - [11] M. AlHajDarwish, H. Kurt, S. Urazhdin, A. Fert, R. Loloee, W.P. Pratt Jr., and J. Bass, *Phys. Rev. Lett.* (in press).
 - [12] S. Urazhdin, W. P. Pratt and J. Bass, *J. Magn. Magn. Mater.* (in press).
 - [13] W. Park, D.V. Baxter, S. Steenwyk, I. Moraru, W.P. Pratt Jr., and J. Bass, *Phys. Rev. B* **62**, 1178 (2000).
 - [14] J. Bass and W. P. Pratt Jr., *J. Magn. Magn. Mat.* **200**, 274 (1999).
 - [15] S. Urazhdin, *Phys. Rev. B* **69**, 134430 (2004).
 - [16] M.L. Polianski and P.W. Brouwer, *Phys. Rev. Lett.* **92**, 026602 (2004).
 - [17] T.Y. Chen, Y. Ji, C.L. Chien, and M.D. Stiles, *Phys. Rev. Lett.* **93**, 026601-1 (2004).
 - [18] B. Ozyilmaz, A.D. Kent, J.Z. Sun, M.J. Rooks, and R.H. Koch, *cond-mat/0403367*.
 - [19] F.B. Mancoff, R.W. Dave, N.D. Rizzo, T.C. Eschrich, B.N. Engel, and S. Tehrani, *Appl. Phys. Lett.* **83**, 1596 (2003).
 - [20] J. Slonczewski, *J. Magn. Magn. Mater.* **159**, L1 (1996); *ibid.* **247**, 324 (2002).
 - [21] L. Berger, *Phys. Rev. B* **54**, 9353 (1996).
 - [22] R. H. Koch, J.A. Katine, and J.Z. Sun, *Phys. Rev. Lett.* **92**, 088302-1 (2004).
 - [23] Z. Li and S. Zhang, *Phys. Rev. B* **69**, 134416 (2004).
 - [24] S. Urazhdin, unpublished.
 - [25] X. Zhu, J.G. Zhu, and R.M. White, *J. Appl. Phys.* **95**, 6630 (2004).
 - [26] J. Miltat, G. Albuquerque, A. Thiaville, C. Vouille, *J. Appl. Phys.* **89**, 6982 (2004).
 - [27] K.J. Lee, A. Deac, O. Redon, J.P. Noziers, and B. Dieny, *cond-mat/0406628*.
 - [28] W. P. Pratt Jr., S.D. Steenwyk, S.Y. Chiang, A.C. Scafer, R. Loloee, and J. Bass, *IEEE Trans. Magn.* **33**, 3505 (1997).
 - [29] B. Nadgorny, R.J. Soulen Jr., M.S. Osofsky, I.I. Mazin, G. Laparade, R.J.M. van de Veerdonk, A.A. Smits, S.F. Cheng, E.F. Skelton, and S.B. Qadri, *Phys. Rev. B* **61**, R3788 (2000).
 - [30] R. Urban, G. Woltersdorf, and B. Heinrich, *Phys. Rev. Lett.* **87**, 217204-1 (2001).